Angewandte Chemie
Eine Zeitschrift der Gesellschaft Deutscher Chemiker

Supporting Information

An Enantioselective e-Nose: An array of Nanoporous Homochiral MOF Films for Stereospecific Sensing of Chiral Odors

*Salih Okur, Peng Qin, Abhinav Chandresh, Chun Li, Zejun Zhang, Ulrich Lemmer, and Lars Heinke**

anie_202013227_sm_miscellaneous_information.pdf

SUPPORTING INFORMATION

Table of Contents

Experimental Setup and Procedures

Additional Data

- X-ray diffractograms
- Scanning electron microscopy images of the samples
- Additional QCM data
- Additional radar plots
- Tables of sensor data
    - Frequency shifts
    - Time constants
- Blank reference measurements
- Additional kNN, LDA and PCA results
- Author's contributions

Setup, Experimental and Data Analysis Procedures

The MOF thin films were prepared in a layer-by-layer fashion, following previously optimized synthesis descriptions.[1]

The achiral SURMOF samples were prepared by alternatively exposing the substrate to the metal node and to the linker solutions, using a spray method.[2] The HKUST-1[2b, 3] MOF thin film was prepared from ethanolic 1 mM copper acetate and ethanolic 0.2 mM trimesic acid (BTC) solutions; Cu(BDC)[4] from ethanolic 1 mM copper acetate and ethanolic 0.2 mM terephthalic acid (BDC) solutions and Cu(BPDC)[4] from ethanolic 1 mM copper acetate and ethanolic 0.2 mM biphenyl dicarboxylic acid (BPDC) solutions.

An isoreticular series of homochiral pillared-layer MOFs of type $Cu_2(Dcam)_2(L)$[5] with identical chiral (1*R*,3*S*)-(+)-camphoric acid (Dcam) layer linker and different pillar linkers L was prepared, see figure 1 or S3. The pillar linkers L are N-donor ligands of type diazabicyclo[2.2.2]octane (dabco), 4,4'-bipyridyl (BiPy) and 1,4-bis(4-pyridyl)benzene (BiPyB), respectively. They are coordinated to the axial positions of the copper complexes, forming pillars of different length, perpendicular to the chiral $Cu_2(Dcam)_2$ layers. The lattice distances are 0.95 nm in [100] and [010] direction as well as 0.95 nm, 1.4 nm and 1.8 nm in [001] direction for the $Cu_2(Dcam)_2$(dabco), $Cu_2(Dcam)_2$(BiPy) and $Cu_2(Dcam)_2$(BiPyB) MOFs, respectively.

All samples were prepared in 30 synthesis cycles. Prior SURMOF synthesis, all gold-coated QCM substrates are functionalized with an 11-mercapto-1-undecanol (MUD) self-assembled monolayers (SAMs), resulting in a [001] crystal orientation of the SURMOF perpendicular to the substrate surface, see Figure S4.

The homochiral and achiral MOFs are denoted as:

- $Cu_2(DCam)_2$(dabco) – chirMOF1
- $Cu_2(DCam)_2$(BiPy) – chirMOF2
- $Cu_2(DCam)_2$(BiPyB) – chirMOF3
- HKUST-1 – achirMOF1
- Cu(BDC) – achirMOF2
- Cu(BPDC) – achirMOF3.

The crystallinity of the MOF samples with the targeted structure was investigated by X-ray diffraction, using a Bruker D8 Discovery with a wavelength of 0.154 nm.

A home-built setup of the 6-channel e-nose system as well as the gas delivery system with a micro-liter syringe pump for odors concentration control was used. The frequency shift of each quartz sensor with an AT-cut and a resonance frequency of 10 MHz was recorded. Each QCM sensor has a round shape with approximately 10 mm diameter. The round Ag top electrode has a diameter of approximately 4 mm and an area 12.5 mm^2. This is the area which is covered by the SURMOFs.

For the QCM data collection, 5V/16MHz ATMega32U4 microcontrollers and open source Pierce oscillator circuits designed by openQCM have been used.[6] One data set, including the frequency shifts of all six sensors, is recorded approximately every 1 – 1.7 second. Temperature and humidity were measured with an Adafruit HTU21D-F sensor. The entire setup has been computer controlled with a program code written in MATLAB.

The odors were evaporated during the injection into the test chamber with a bulb filament heater at 60°C. In test experiments, the entire evaporation of the injected VOCs was confirmed. Two valves with mass flowmeters were used to transfer the evaporated odorant vapors through the test cell, which is a stainless steel cylindrical test cell with a volume of 34 L. The temperature was kept constant at 34 ± 1 °C, to prevent condensation of vapor molecules on the wall of the test chamber. The different VOCs with concentrations of 10 ppm, 50 ppm and 100 ppm have been injected sequentially into the sample evaporator attached to the test cell with a computer-controlled microliter syringe (Hamilton Model 700).

For the desorption/activation process, the test chamber was purged with dry air (20% O_2, 80% N_2, <1 ppm H_2O) with a flow rate of 15 L min^{-1} for 30 min before introducing the evaporated VOCs. In the experiments, each cycle consists of approximately 17-22 min for adsorption and 30 min for desorption, i.e. 50 min in total.

The initial resonance frequency values of each sensor were determined at the beginning of the experiment as an average value of 10 measurements. The shift in the resonance frequency due to the uptake of the targeted molecules was recorded for each sensor during the experiments.

The change of the mass density (Δm) of the film on the surface can be calculated by the Sauerbrey equation[7]:

$$\Delta m = \frac{A\sqrt{\mu\rho}}{2\,{f_0}^2} \times \Delta f$$

where f_0 denotes the resonance frequency of the fundamental mode of the QCM crystal, Δf is the frequency change, A the surface area, ρ the density of the crystal (2.684 g cm^{-3}) and μ is the shear modulus of quartz (2.947×10^{11} g cm^{-1} s^{-2}). Due to the very small energy dissipation of such SURMOFs[8], the application of the (uncorrected) Sauerbrey equation is generally enabled.[9]

In the QCM data, a small baseline drift cannot be avoided. Here, we observe a small drift in the range of 10 Hz per hour or less. To avoid that the baseline drift affects the sensor results, the baseline is corrected so that each molecular uptake starts with a frequency shift of 0 (see data in Fig. 2 and S6). The baseline drift is significantly smaller than the odor signals.

The setup is shown in Figure S1 and S2. All the sensors are inside the chamber where the gas is mixed by the ventilator, resulting in similar gas composition (with equal vapor concentration) at each sensor. During both desorption or cleaning the chamber, the 34 L test cell is under constant gas flow. During the adsorption phase, both valves are closed, the odor vapor is distributed homogenously by the ventilator. Valve 1 and valve 2 (see Figure S1) are used for purging, not for transfer of the evaporated odorants. Switching the valves did not cause any pressure build-up in the cell, potentially affecting the resonance frequency of the sensors.

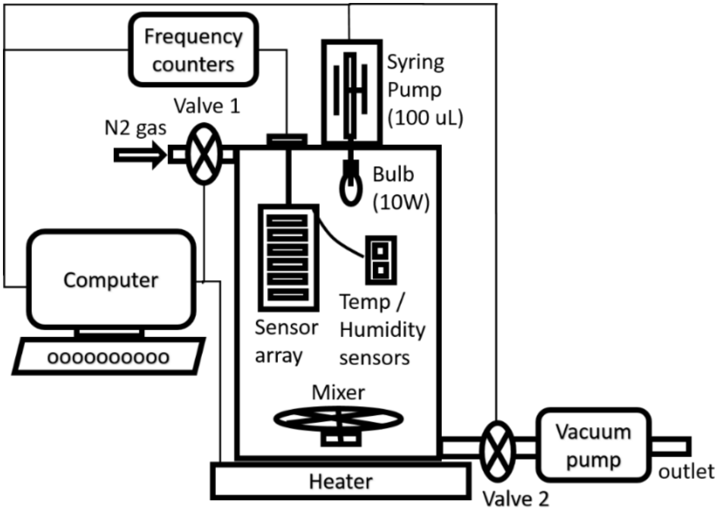

Figure S1: Sketch of the experimental setup. The e-nose sensor array is in the chamber which can be purged with dry air or nitrogen. The analyte is injected by the syringe and evaporated in on the bulb at about 60°C. The gas and vapor in the chamber is mixed by the (mixer) ventilator.

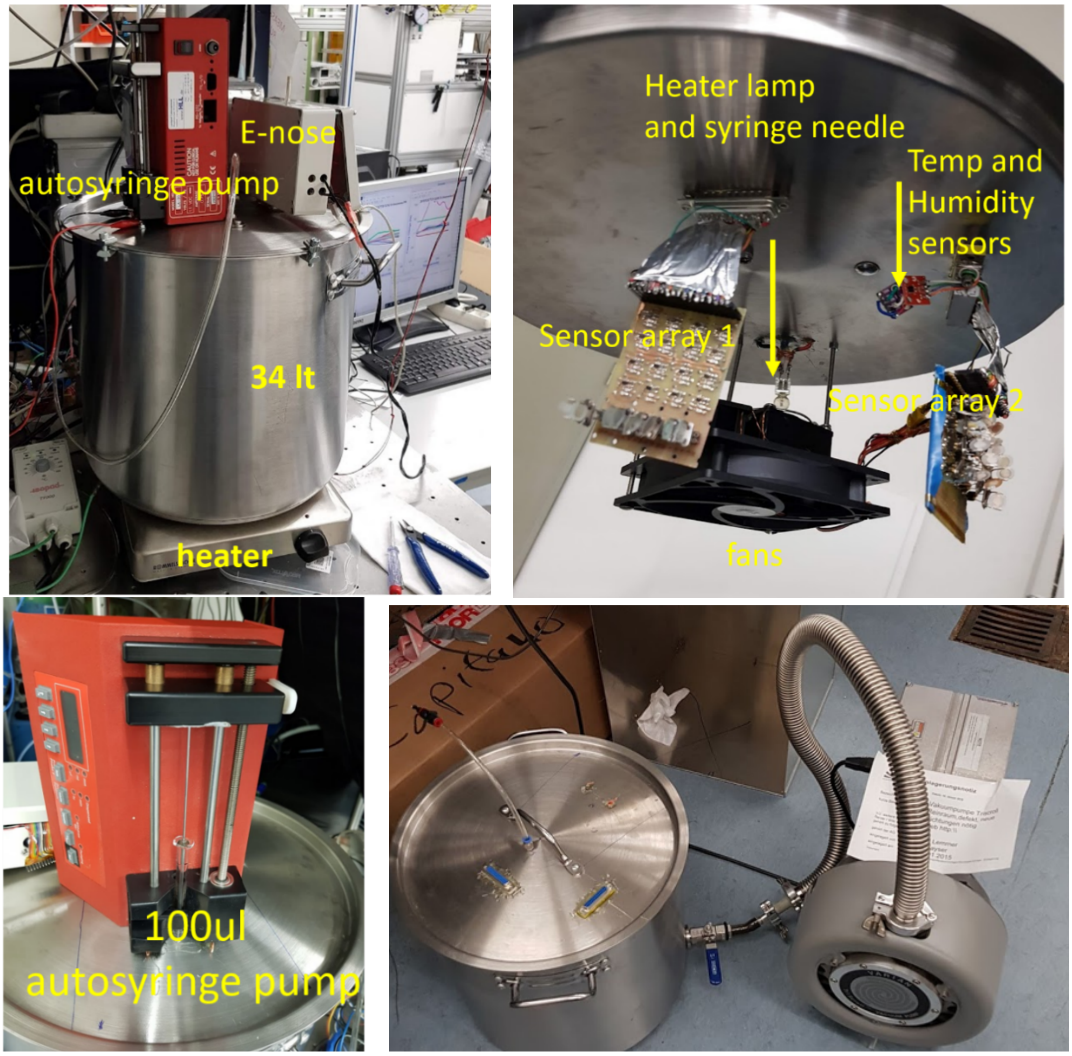

Figure S2: Photographs of the experimental setup. The individual components are labelled. The experiments were performed with sensor array 2 (picture top right). The circuit board of this sensor array has a size of 6 cm × 9 cm and the QCM sensors point up to 2 cm out, so the total volume of the sensor array is about 100 cm^3.

Standard machine learning algorithms, that are k-Nearest Neighbor (k-NN)[10] algorithms written in *python*, have been used for classifying the sensing data. For each enantiomer, 40 data points at the end of the odor exposure period are used for the kNN classification. This makes 400 data points for all 10 molecules, where each data point includes the frequency shift values of all 6 six sensors.

Please note, for the analysis in Figure 4c and S11c, the data points were collected in subsequent time intervals (~0-1min, ~1-2min, ~2-3min, etc. until the end of the vapor exposure) to investigate the transient change of the classifying accuracy. (There, also 40 points per molecule were used, resulting again in 400 data points where each point includes the data of all 6 sensors.)

In addition, for the analysis of the data from only half the sensor array, that is the data from only the 3 chiral sensors or from only the 3 achiral sensors, see Figure 4b and 4c as well as S11, each data point at a certain time includes only the data of 3 sensors, either chirMOF1, chirMOF2 and chirMOF3 or achirMOF1, achirMOF2 and achirMOF3.

The k-value in kNN was set to 20 (corresponding $400^{0.5}$) and no significant variation of the results was found for small variations (e.g. $k = 10$ or $k = 30$). 1,000-fold cross-validation was used for the classification with 90 % of the data points used as training sets (i.e. 360 points) and 10 % as test sets (40 points).

For kNN-analysis of e-nose data, different metric functions (or distance functions) can be used, see e.g. ref.[11]. Here, we use a Euclidean metric function with an activation threshold to respect small variations of the data, also referred to as Rectified Linear Unit (ReLU) activation function or linear metrics with activation function.[12] As threshold value we chose the average standard deviation of the data at the 10 ppm range, 0.1 Hz.

Additional Data

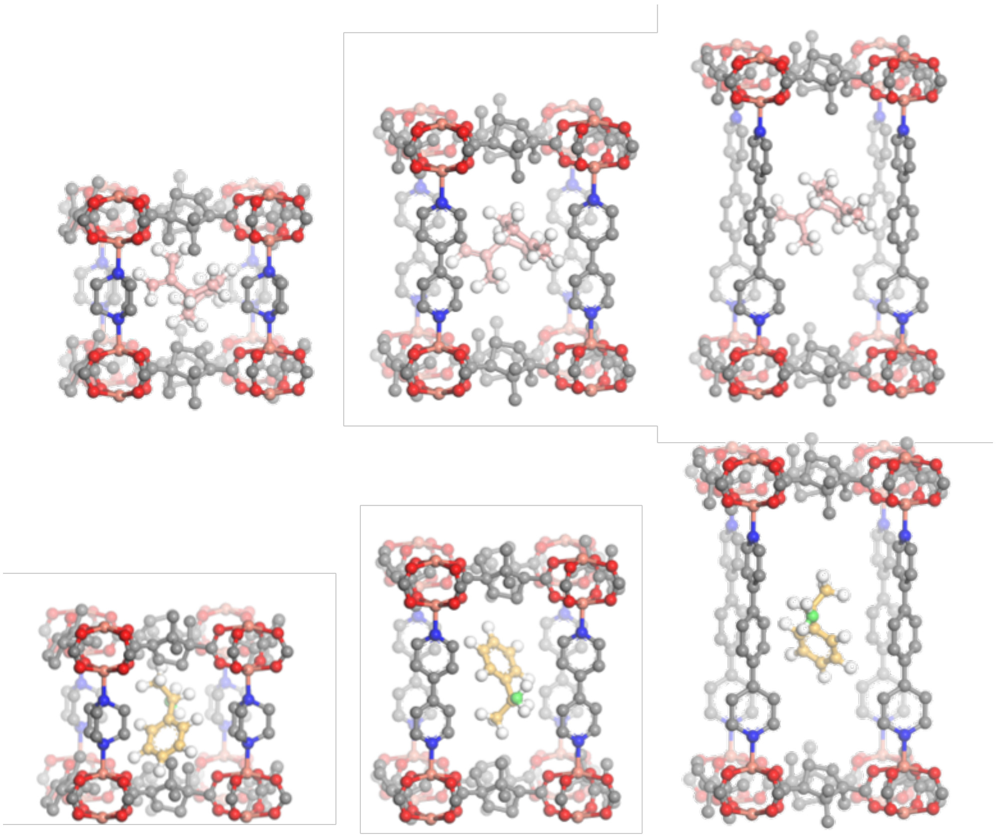

Figure S3: Sketch of chirMOF1 (left), chirMOF2 (center) and chirMOF3 (right) with one limonene (top row) and one phenylethylamine (bottom row) molecule in the center of the pores. The structures show that there is sufficient space in the pores for the uptake of the molecules.

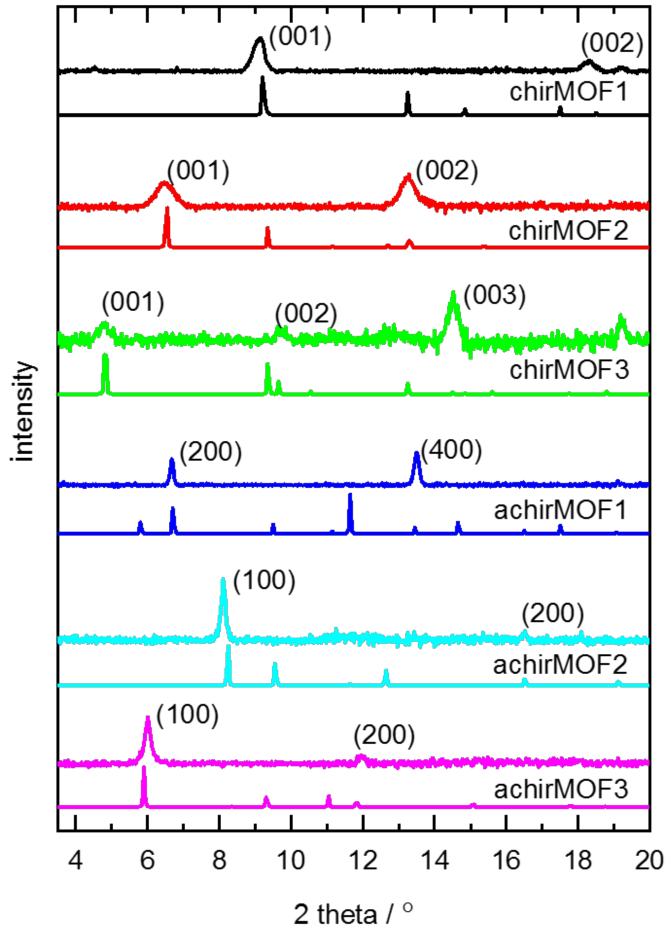

Figure S4: The X-ray diffractograms of the MOF thin films. The MOF names as well as the diffraction peaks are labelled. The calculated XRDs of the targeted structures are below the XRDs of the samples. The data indicates crystalline, oriented growth of the MOF films with the targeted structure.

a)

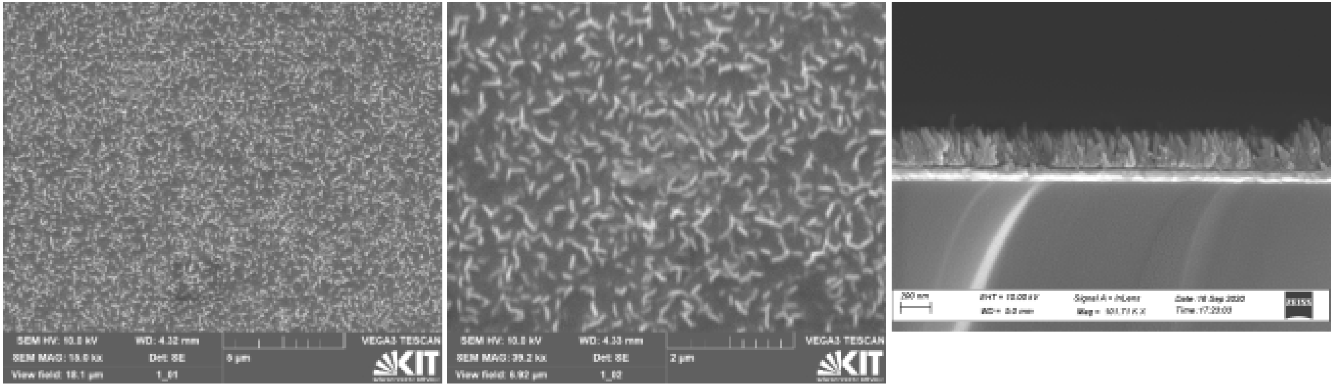
SEM HV: 10.0 kV
WD: 4.32 mm
VEGA3 TESCAN
SEM MAG: 15.0 kx
Det: SE
5 µm
View field: 18.1 µm
1_01
KIT
SEM HV: 10.0 kV
WD: 4.33 mm
VEGA3 TESCAN
SEM MAG: 39.2 kx
Det: SE
2 µm
View field: 6.92 µm
1_02
KIT

b)

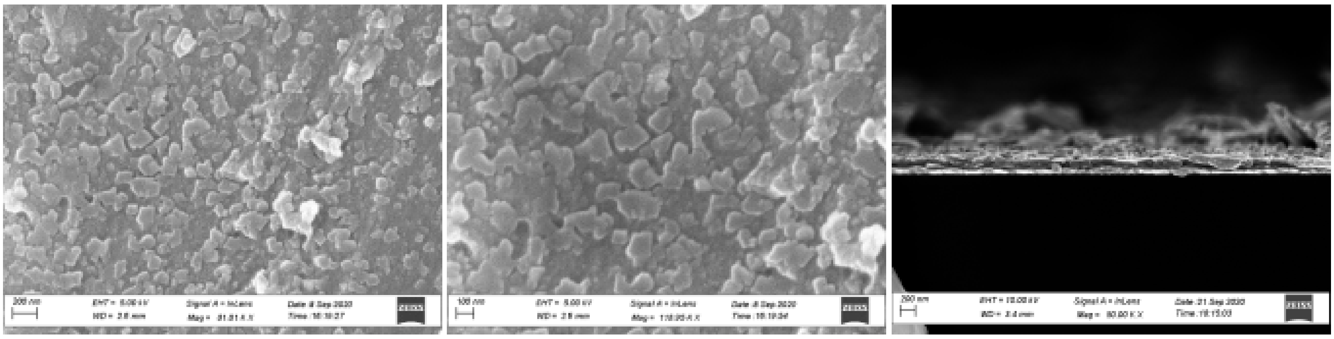

c)

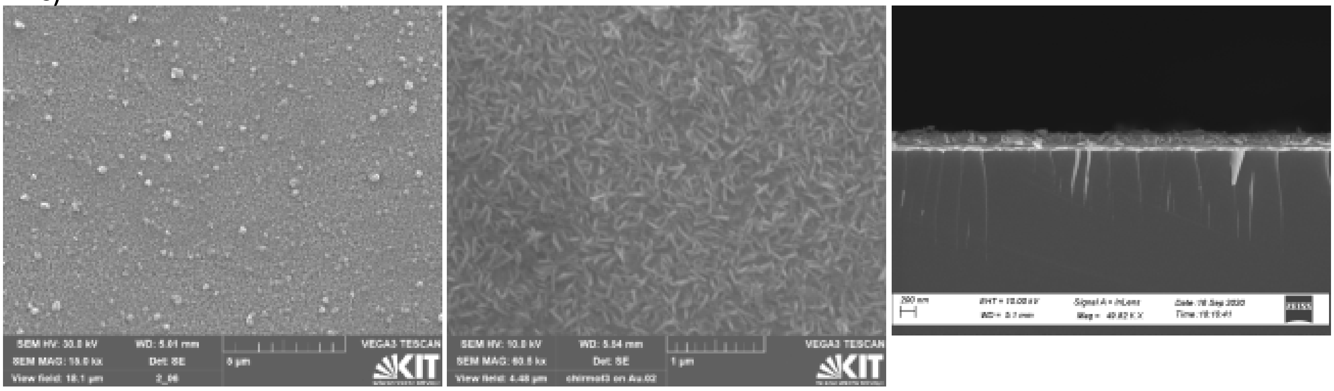
SEM HV: 30.0 kV
WD: 5.01 mm
VEGA3 TESCAN
SEM MAG: 15.0 kx
Det: SE
5 µm
View field: 18.1 µm
2_06
KIT
SEM HV: 10.0 kV
WD: 5.54 mm
VEGA3 TESCAN
SEM MAG: 60.5 kx
Det: SE
1 µm
View field: 4.48 µm
KIT

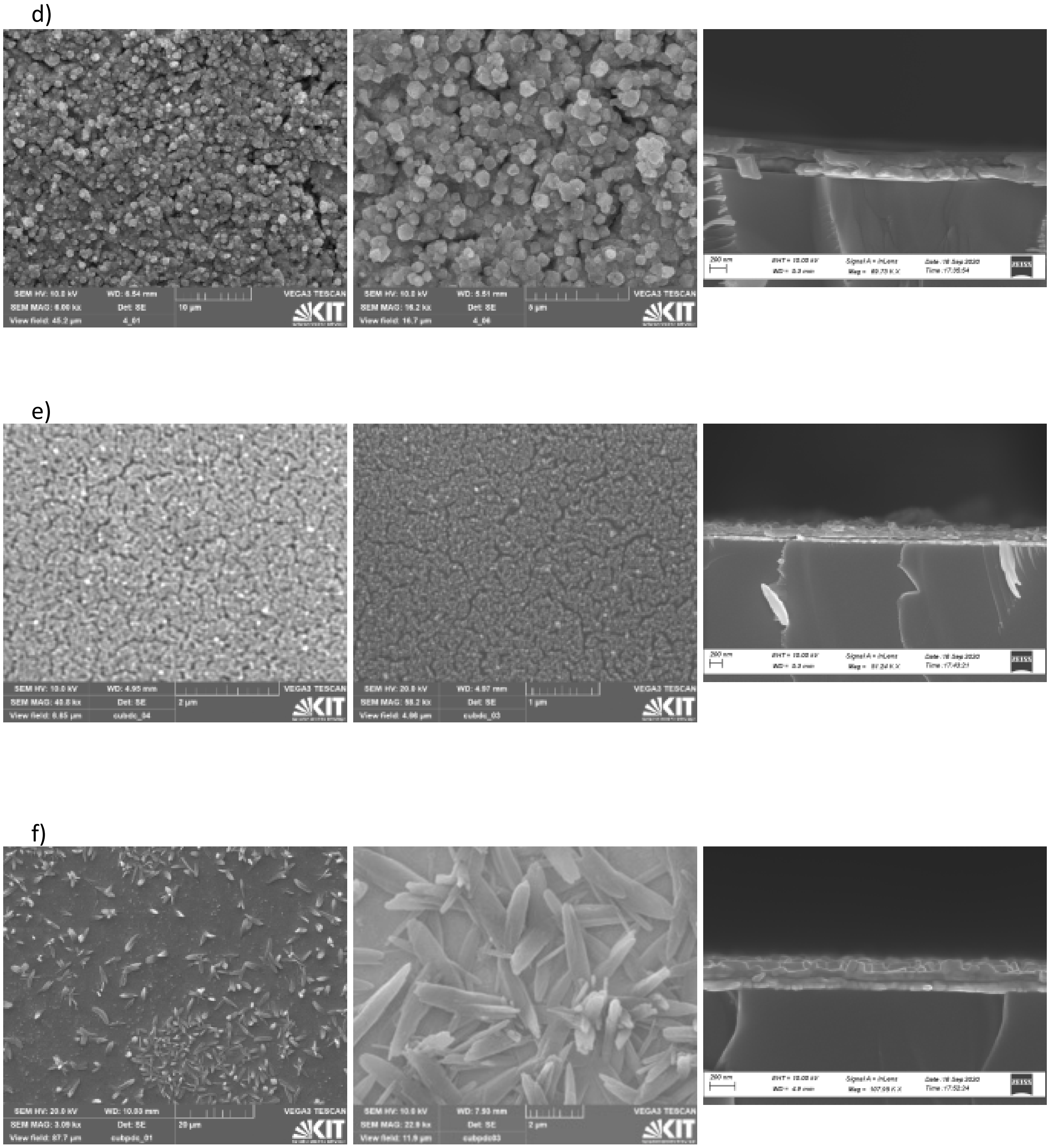

Figure S5: Scanning electron microscopy (SEM) images of the samples. a) chirMOF1, b) chirMOF2, c) chirMOF3, d) achirMOF1, e) achirMOF2 and f) achirMOF3. The images show the top view, only the images on the right-hand side show the side views of the broken sensors. The top-view images show typical morphologies for such SURMOFs.[13] Please note, the surface roughness of these samples were not optimized, for instance by ultrasonication,[14] resulting in rather rough films. The cross-section images allow estimations of the SURMOF thicknesses, which are in the range of 100-200 nm.

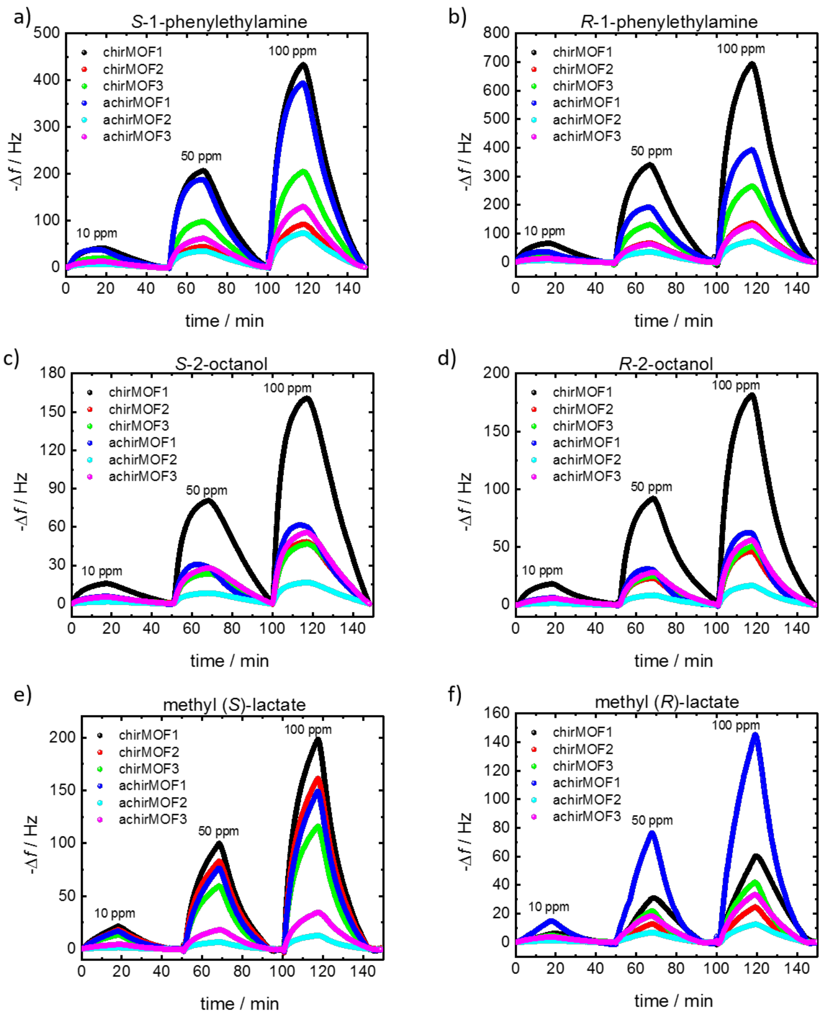

Figure S6. QCM data of the uptake of the enantiopure molecules as function of time. The frequency shifts of the sensors with the different SURMOF coatings are shown in different color with the color code given in the legend. The sensor array is exposed first to 10 ppm, then to 50 ppm and to 100 ppm of the odors. The odor molecules are labelled.

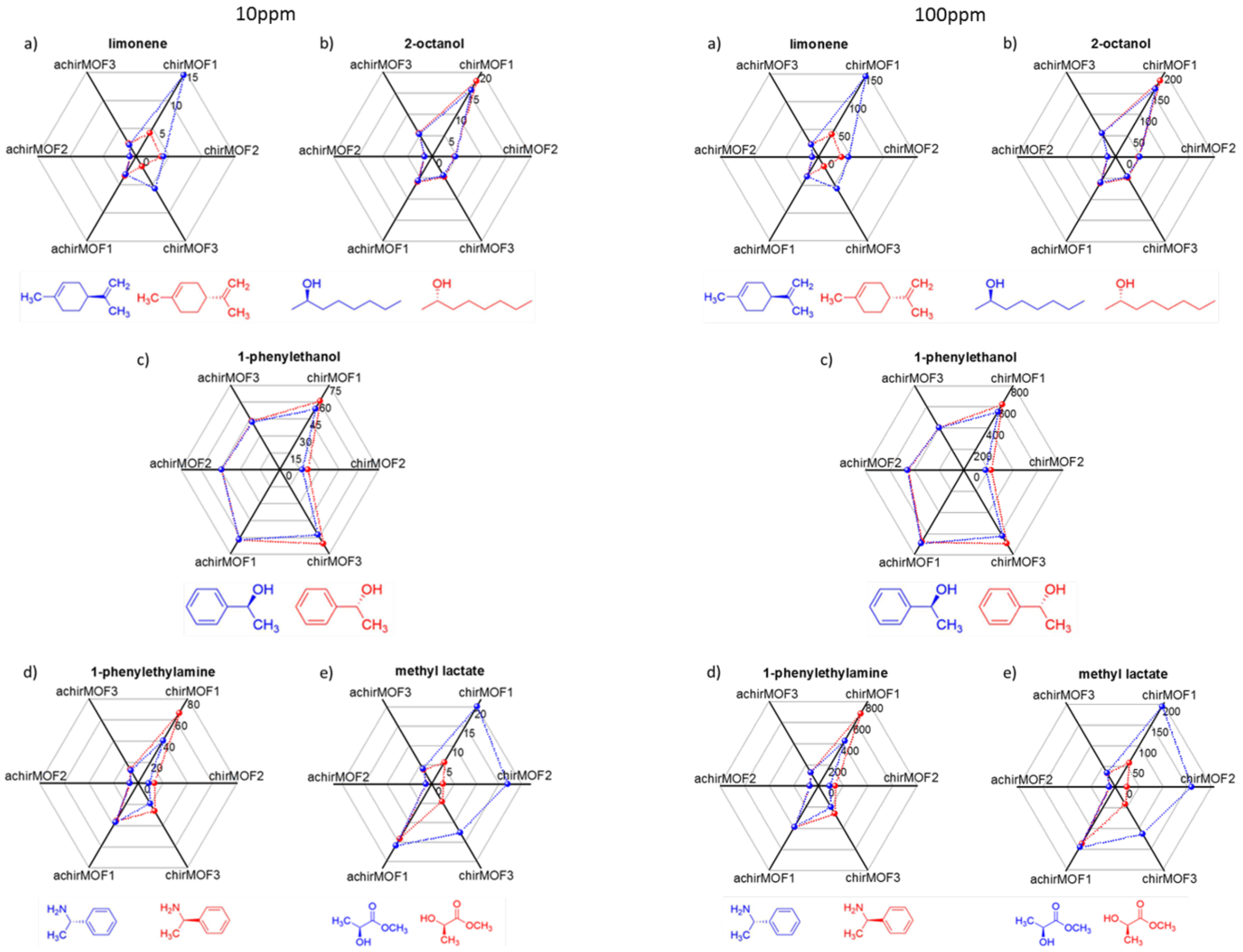

Figure S7: Radar plots of the sensor response to the exposure of a) *R*-and *S*-limonene, b) *R*-and *S*-2-octanol, c) *R*-and *S*-1-phenylethanol d) *R*-and *S*-1-phenylethylamine and e) methyl *R*- and *S*-lactate. The *R*-enantiomers are plotted in red, *S*-enantiomers are plotted in blue. The concentration is **10 ppm on the left hand side, and it is 100 ppm on the right-hand side**. Axes of the radar plots are the negative values of the recorded frequency shifts in Hz at the end of each uptake period, averaged over 40 points, see table S1. These values correspond to the averaged maximum signals. The molecular structure of the *R*- and *S*-enantiomers are shown below the radar plots.

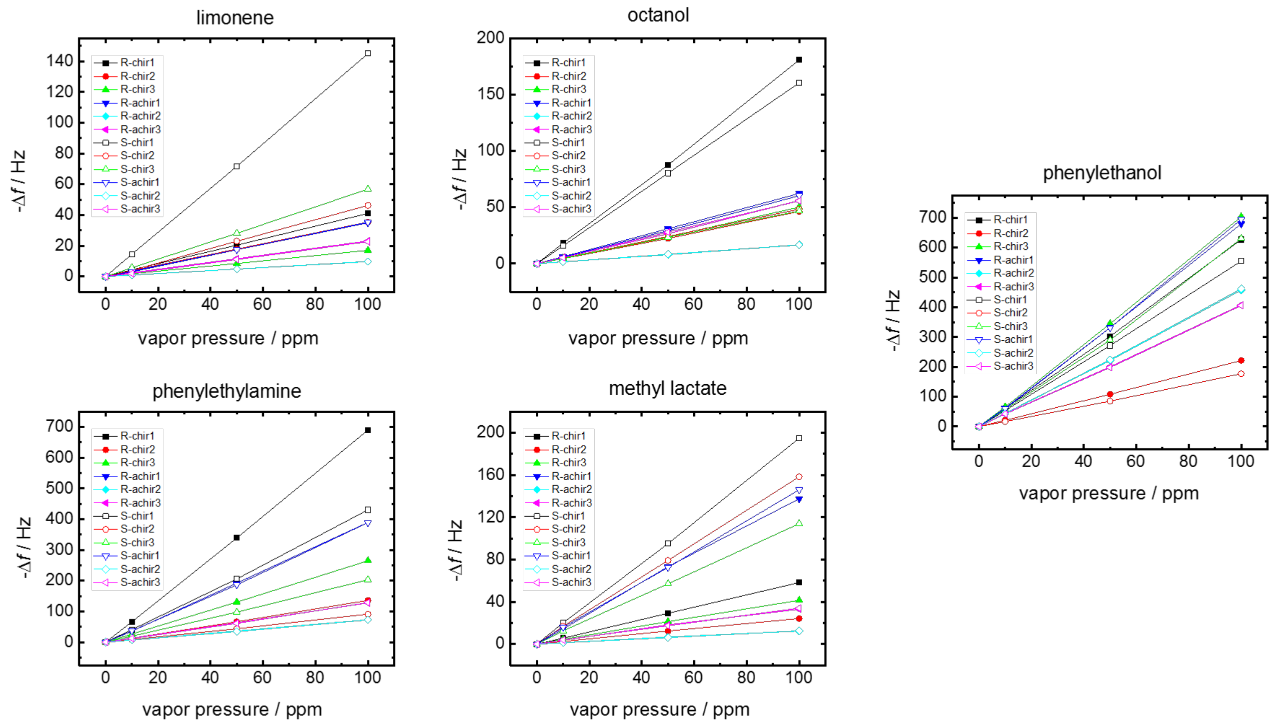

Figure S8: Negative values of the frequency shift *vs*. vapor pressure. The frequency shift (which is proportional to the mass change, see Sauerbrey equation above) shows an essentially linear dependence on the vapor pressure in the range below 100 ppm for all molecules in all SURMOF sensors. Noteworthy, each sensor shows different slopes for different molecules and, more importantly, the same molecule shows different slopes in different sensors. Similar to ref.[15], the adsorption isotherms of the different isomers at small concentrations show different linear slopes in the chiral MOF films, indicating different affinities. The data is shown in table S1. For many sensors, the sensor responses are essentially in equilibrium at the end of the adsorption process (i.e. more than 90% of the equilibrium loading is reached), see also the time constants in table S2. However, for some sensors the equilibrium state is not fully reached and the shown data do not represent an adsorption isotherm.

The large frequency shifts, e.g. for phenylethanol and phenylethylamine, are a result of strong attractive interaction between the guest and the MOF host. It should be stressed that enantioselective adsorption and its enantioselective molecular interaction in MOFs is understood in detail only for a few examples so far[16] and details of the enantioselective molecular interaction, although highly interesting and worth studying to improve the e-nose performance, are beyond the scope of the present work. We suppose phenylethylamine and phenylethanol have attractive interaction based on its polar group via dipole interaction and hydrogen bonding and based on its phenyl ring via van-der-Waals and aryl interactions with the organic and inorganic parts of the MOF. Moreover, their rather low volatilities also contribute to large adsorption capacities. In line with the low vapor pressures of phenylethanol and phenylethylamine, large sensor responses are observed for these molecules. Since the vapor pressure of phenylethanol at 100ppm is close to the saturation vapor pressure at 22°C (15 Pa[17], corresponding to 150 ppm), a loading close to the maximum loading is expected and the adsorption isotherm is no more in the (low pressure) Henry regime. For the enantioselective adsorption, it can be speculated that, e.g., for phenylethylamine in chirMOF-1, the higher adsorption amount of the *R*-isomer compared to the *S*-isomer is caused by the better match of the molecular shape with the attractive adsorption sites.

Table S1. Data of sensor responses in Hz of the individual sensors for the individual odor molecules. The data is averaged over 40 points at the end of each odor-exposure-step (= adsorption step). The standard deviations are given.

	limonene		**2-octanol**		**methyl lactate**		**1-phenylethylamine**		**1-phenylethanol**	
	R	***S***	***R***	***S***	***R***	***S***	***R***	***S***	***R***	***S***
10 ppm										
chirMOF1	4.16 ± 0.04	14.43 ± 0.13	17.85 ± 0.14	15.72 ± 0.05	5.59 ± 0.11	20.14 ± 0.21	66.37 ± 0.09	40.24 ± 0.18	60.86 ± 0.18	53.86 ± 0.06
chirMOF2	3.79 ± 0.04	4.16 ± 0.07	4.50 ± 0.02	4.67 ± 0.02	2.49 ± 0.05	16.87 ± 0.17	13.06 ± 0.02	8.40 ± 0.05	21.12 ± 0.04	16.87 ± 0.04
chirMOF3	1.75 ± 0.03	5.69 ± 0.05	4.83 ± 0.05	4.47 ± 0.03	4.56 ± 0.08	12.62 ± 0.11	26.26 ± 0.05	19.27 ± 0.09	65.74 ± 0.18	57.73 ± 0.05
achirMOF1	3.42 ± 0.03	3.17 ± 0.06	5.99 ± 0.07	5.73 ± 0.03	14.25 ± 0.26	15.99 ± 0.15	35.69 ± 0.23	36.90 ± 0.05	62.31 ± 0.05	62.16 ± 0.66
achirMOF2	0.93 ± 0.02	0.97 ± 0.02	1.62 ± 0.03	1.58 ± 0.02	1.29 ± 0.02	1.33 ± 0.03	7.12 ± 0.03	6.97 ± 0.04	44.27 ± 0.11	44.42 ± 0.04
achirMOF3	2.32 ± 0.02	2.05 ± 0.03	5.50 ± 0.07	5.29 ± 0.03	3.73 ± 0.04	3.96 ± 0.03	13.11 ± 0.04	12.08 ± 0.08	42.96 ± 0.24	42.20 ± 0.18
50 ppm										
chirMOF1	19.97 ± 0.06	71.69 ± 0.86	89.61 ± 0.68	79.59 ± 0.37	29.16 ± 0.38	95.09 ± 0.64	339.29 ± 1.52	203.52 ± 0.79	303.37 ± 0.07	271.94 ± 0.07
chirMOF2	17.46 ± 0.05	22.42 ± 0.50	22.79 ± 0.14	24.06 ± 0.06	12.38 ± 0.13	79.22 ± 0.51	66.55 ± 0.35	42.99 ± 0.22	108.79 ± 0.05	85.49 ± 0.04
chirMOF3	8.25 ± 0.03	28.26 ± 0.30	24.46 ± 0.22	23.22 ± 0.10	21.25 ± 0.19	57.09 ± 0.34	130.33 ± 0.64	96.21 ± 0.42	344.34 ± 0.41	289.54 ± 0.32
achirMOF1	17.08 ± 0.04	16.99 ± 0.37	31.00 ± 0.05	29.79 ± 0.23	73.36 ± 0.79	72.65 ± 0.57	192.19 ± 0.29	186.54 ± 0.35	331.64 ± 0.63	332.79 ± 0.37
achirMOF2	4.71 ± 0.02	4.84 ± 0.04	8.18 ± 0.06	8.23 ± 0.05	6.60 ± 0.05	6.18 ± 0.04	36.01 ± 0.20	34.11 ± 0.15	222.08 ± 0.10	224.15 ± 0.07
achirMOF3	11.35 ± 0.03	10.83 ± 0.25	27.33 ± 0.25	27.33 ± 0.25	18.24 ± 0.12	17.40 ± 0.10	63.12 ± 0.35	60.21 ± 0.34	199.95 ± 0.49	197.84 ± 0.20
100 ppm										
chirMOF1	40.79 ± 0.08	144.99 ± 1.05	179.63 ± 0.75	160.18 ± 0.32	58.21 ± 0.93	194.91 ± 1.02	683.33 ± 4.17	425.22 ± 3.07	621.57 ± 2.54	550.85 ± 1.57
chirMOF2	35.20 ± 0.07	45.99 ± 0.44	46.06 ± 0.10	48.34 ± 0.06	24.20 ± 0.26	158.39 ± 0.85	134.53 ± 0.90	89.78 ± 0.78	220.04 ± 0.90	175.88 ± 0.53
chirMOF3	16.91 ± 0.04	56.88 ± 0.38	49.72 ± 0.26	46.58 ± 0.11	41.44 ± 0.37	113.99 ± 0.56	262.01 ± 1.69	200.44 ± 1.60	694.25 ± 4.07	623.17 ± 2.69
achirMOF1	34.75 ± 0.04	35.15 ± 0.33	62.49 ± 0.05	60.71 ± 0.23	137.53 ± 1.61	146.13 ± 0.95	389.81 ± 1.63	389.08 ± 2.04	679.64 ± 1.54	693.28 ± 1.21
achirMOF2	9.59 ± 0.02	9.77 ± 0.05	16.60 ± 0.08	16.54 ± 0.05	12.35 ± 0.12	12.54 ± 0.06	71.93 ± 0.49	71.45 ± 0.60	453.23 ± 2.05	458.04 ± 1.46
achirMOF3	23.02 ± 0.03	22.55 ± 0.21	55.57 ± 0.26	55.61 ± 0.12	33.07 ± 0.28	33.99 ± 0.20	126.40 ± 0.92	126.69 ± 1.14	402.90 ± 2.18	402.03 ± 1.83

Table S2. Time constants of the sensor responses for the different molecules. The time constant τ is determined by a mono-exponential fit to the data (~exp(-*t*/τ), see Fig. S9 The units are min. The average is 7.2 min for all sensors, molecules and concentrations. For 10 ppm, the average is 9.5 min, 6.3 min for 50 ppm and 5.8 min for 100 ppm.

These uptake time constants are in line with previously determined time constants for VOC uptake by similar achiral and chiral SURMOF films.[18] We believe the reason for the slow uptake, in comparison to very fast uptake in defect-free MOF films, are defects, like surface defects, slowing down the mass transfer.[19]

	limonene		**2-octanol**		**methyl lactate**		**1-phenylethylamine**		**1-phenylethanol**	
	R	***S***	***R***	***S***	***R***	***S***	***R***	***S***	***R***	***S***
10 ppm										
chirMOF1	9.04	20.36	5.98	5.72	4.36	25.33	5.63	5.06	3.65	3.41
chirMOF2	10.58	21.89	3.77	4.31	4.36	25.87	6.33	6.43	2.99	3.11
chirMOF3	10.6	18.29	8.02	5.4	14.57	16.62	5.95	5.21	3.31	3.29
achirMOF1	10.6	16.82	8.89	6.74	10.69	22.56	3.83	3.39	2.15	1.77
achirMOF2	8.99	25.6	7.83	8.85	22.46	16.11	6.37	5.37	3.99	3.75
achirMOF3	8.18	20.9	12.05	6.79	13.99	13.13	7.13	6.16	5.29	9.89
50 ppm										
chirMOF1	4.51	7.49	5.04	4.29	9.92	8.69	5.5	4.75	3.15	3.09
chirMOF2	4.88	4.4	4.77	4.17	14.32	7.99	6.17	5.77	3.26	3.36
chirMOF3	5.17	9.19	5.68	4.32	12.69	7.91	5.85	5.01	3.59	3.73
achirMOF1	4.68	14.37	4.48	3.39	20.19	9.87	4.64	4.17	2.8	2.84
achirMOF2	4.67	10.05	5.58	4.8	20.35	7.02	6.01	4.98	3.28	3.26
achirMOF3	4.7	4.3	6.63	5.02	7.69	9.21	6.36	5.31	3.46	3.46
100 ppm										
chirMOF1	3.83	5.86	4.7	4.02	22.34	6.37	5.37	5.64	4.02	3.69
chirMOF2	3.98	4.93	4.65	3.94	14.61	6.6	6.07	6.49	4.15	4.06
chirMOF3	4.22	6.97	5.75	4.27	10.39	6.39	5.28	5.75	4.64	4.31
achirMOF1	3.87	4.93	4.04	3.5	14.37	7.57	4.84	5.08	3.63	3.57
achirMOF2	3.87	7.02	4.89	4.15	10.47	6.08	5.86	5.82	4.18	3.9
achirMOF3	3.82	4.91	4.91	4.16	10.2	7.03	6.23	6.24	4.38	4.02

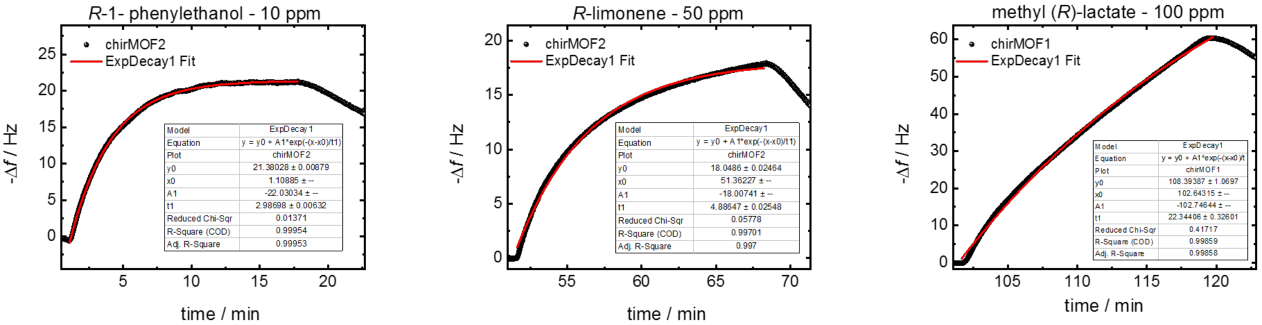

Model	ExpDecay1
Equation	y = y0 + A1*exp(-(x-x0)/t1)
Plot	chirMOF2
y0	21.38028 ± 0.00879
x0	1.10885 ± --
A1	-22.03034 ± --
t1	2.98698 ± 0.00632
Reduced Chi-Sqr	0.01371
R-Square (COD)	0.99954
Adj. R-Square	0.99953

Model	ExpDecay1
Equation	y = y0 + A1*exp(-(x-x0)/t1)
Plot	chirMOF2
y0	18.0486 ± 0.02464
x0	51.36227 ± --
A1	-18.00741 ± --
t1	4.88647 ± 0.02548
Reduced Chi-Sqr	0.05778
R-Square (COD)	0.99701
Adj. R-Square	0.997

Model	ExpDecay1
Equation	y = y0 + A1*exp(-(x-x0)/t
Plot	chirMOF1
y0	108.39387 ± 1.0697
x0	102.64315 ± --
A1	-102.74644 ± --
t1	22.34406 ± 0.32601
Reduced Chi-Sqr	0.41717
R-Square (COD)	0.99859
Adj. R-Square	0.99858

Figure S9: Three examples of fitting the experimental sensor data with a mono-exponential decay function. The sensors, VOCs and concentrations are labelled. All experimental data can be reasonably described by the fit function and the time constant can be extracted.

The examples are representative for the entire data. On the left-hand side, the uptake is relatively fast. The center shows an uptake with an average time constant and on the right-hand side, the uptake time constants is among the largest values.

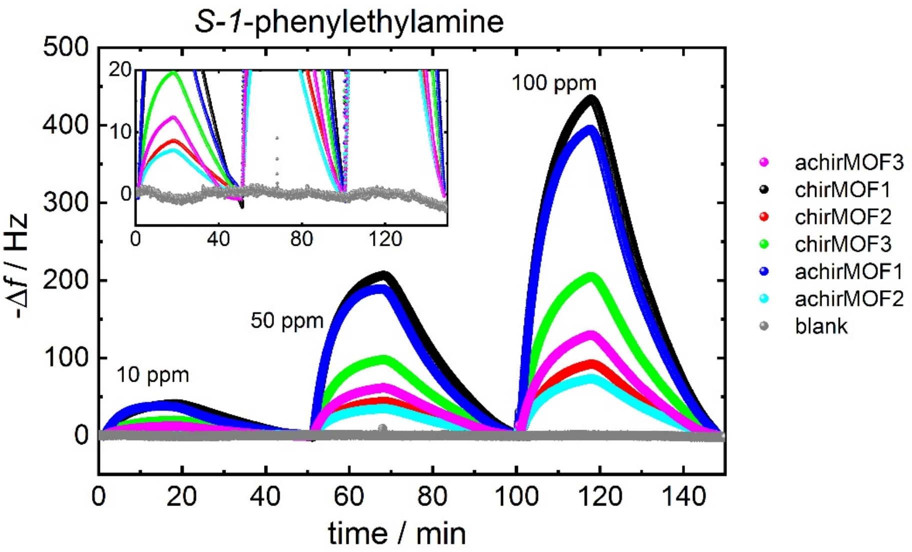

Figure S10: QCM data of blank reference sensor (grey) in comparison to the sensor responses of the SURMOF sensors. The inset shows a zoom-in. The blank sensor shows no significant response to the phenylethylamine exposure. Standard deviation of the sensor signal is 0.7 Hz, averaged over the entire experiment of 2.5 h.

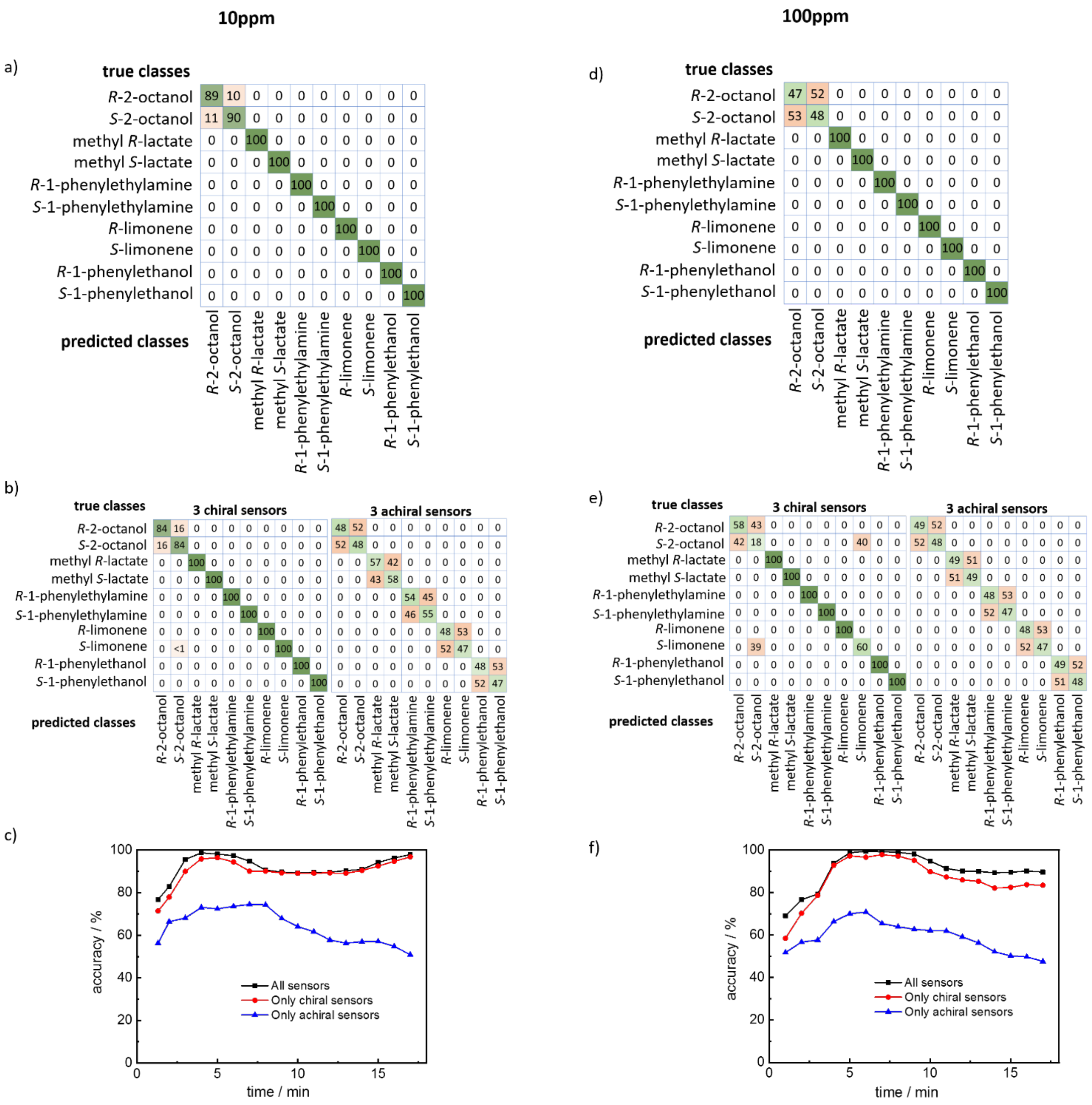

a) 10ppm

true classes \ predicted classes	*R*-2-octanol	*S*-2-octanol	methyl *R*-lactate	methyl *S*-lactate	*R*-1-phenylethylamine	*S*-1-phenylethylamine	*R*-limonene	*S*-limonene	*R*-1-phenylethanol	*S*-1-phenylethanol
R-2-octanol	89	10	0	0	0	0	0	0	0	0
S-2-octanol	11	90	0	0	0	0	0	0	0	0
methyl *R*-lactate	0	0	100	0	0	0	0	0	0	0
methyl *S*-lactate	0	0	0	100	0	0	0	0	0	0
R-1-phenylethylamine	0	0	0	0	100	0	0	0	0	0
S-1-phenylethylamine	0	0	0	0	0	100	0	0	0	0
R-limonene	0	0	0	0	0	0	100	0	0	0
S-limonene	0	0	0	0	0	0	0	100	0	0
R-1-phenylethanol	0	0	0	0	0	0	0	0	100	0
S-1-phenylethanol	0	0	0	0	0	0	0	0	0	100

b) 10ppm

true classes \ predicted classes	3 chiral sensors										3 achiral sensors									
	R-2-octanol	*S*-2-octanol	methyl *R*-lactate	methyl *S*-lactate	*R*-1-phenylethylamine	*S*-1-phenylethylamine	*R*-limonene	*S*-limonene	*R*-1-phenylethanol	*S*-1-phenylethanol	*R*-2-octanol	*S*-2-octanol	methyl *R*-lactate	methyl *S*-lactate	*R*-1-phenylethylamine	*S*-1-phenylethylamine	*R*-limonene	*S*-limonene	*R*-1-phenylethanol	*S*-1-phenylethanol
R-2-octanol	84	16	0	0	0	0	0	0	0	0	48	52	0	0	0	0	0	0	0	0
S-2-octanol	16	84	0	0	0	0	0	0	0	0	52	48	0	0	0	0	0	0	0	0
methyl *R*-lactate	0	0	100	0	0	0	0	0	0	0	0	0	57	42	0	0	0	0	0	0
methyl *S*-lactate	0	0	0	100	0	0	0	0	0	0	0	0	43	58	0	0	0	0	0	0
R-1-phenylethylamine	0	0	0	0	100	0	0	0	0	0	0	0	0	0	54	45	0	0	0	0
S-1-phenylethylamine	0	0	0	0	0	100	0	0	0	0	0	0	0	0	46	55	0	0	0	0
R-limonene	0	0	0	0	0	0	100	0	0	0	0	0	0	0	0	0	48	53	0	0
S-limonene	0	<1	0	0	0	0	0	100	0	0	0	0	0	0	0	0	52	47	0	0
R-1-phenylethanol	0	0	0	0	0	0	0	0	100	0	0	0	0	0	0	0	0	0	48	53
S-1-phenylethanol	0	0	0	0	0	0	0	0	0	100	0	0	0	0	0	0	0	0	52	47

d) 100ppm

true classes \ predicted classes	*R*-2-octanol	*S*-2-octanol	methyl *R*-lactate	methyl *S*-lactate	*R*-1-phenylethylamine	*S*-1-phenylethylamine	*R*-limonene	*S*-limonene	*R*-1-phenylethanol	*S*-1-phenylethanol
R-2-octanol	47	52	0	0	0	0	0	0	0	0
S-2-octanol	53	48	0	0	0	0	0	0	0	0
methyl *R*-lactate	0	0	100	0	0	0	0	0	0	0
methyl *S*-lactate	0	0	0	100	0	0	0	0	0	0
R-1-phenylethylamine	0	0	0	0	100	0	0	0	0	0
S-1-phenylethylamine	0	0	0	0	0	100	0	0	0	0
R-limonene	0	0	0	0	0	0	100	0	0	0
S-limonene	0	0	0	0	0	0	0	100	0	0
R-1-phenylethanol	0	0	0	0	0	0	0	0	100	0
S-1-phenylethanol	0	0	0	0	0	0	0	0	0	100

e) 100ppm

true classes \ predicted classes	3 chiral sensors										3 achiral sensors									
	R-2-octanol	*S*-2-octanol	methyl *R*-lactate	methyl *S*-lactate	*R*-1-phenylethylamine	*S*-1-phenylethylamine	*R*-limonene	*S*-limonene	*R*-1-phenylethanol	*S*-1-phenylethanol	*R*-2-octanol	*S*-2-octanol	methyl *R*-lactate	methyl *S*-lactate	*R*-1-phenylethylamine	*S*-1-phenylethylamine	*R*-limonene	*S*-limonene	*R*-1-phenylethanol	*S*-1-phenylethanol
R-2-octanol	58	43	0	0	0	0	0	0	0	0	49	52	0	0	0	0	0	0	0	0
S-2-octanol	42	18	0	0	0	0	0	40	0	0	52	48	0	0	0	0	0	0	0	0
methyl *R*-lactate	0	0	100	0	0	0	0	0	0	0	0	0	49	51	0	0	0	0	0	0
methyl *S*-lactate	0	0	0	100	0	0	0	0	0	0	0	0	51	49	0	0	0	0	0	0
R-1-phenylethylamine	0	0	0	0	100	0	0	0	0	0	0	0	0	0	48	53	0	0	0	0
S-1-phenylethylamine	0	0	0	0	0	100	0	0	0	0	0	0	0	0	52	47	0	0	0	0
R-limonene	0	0	0	0	0	0	100	0	0	0	0	0	0	0	0	0	48	53	0	0
S-limonene	0	39	0	0	0	0	0	60	0	0	0	0	0	0	0	0	52	47	0	0
R-1-phenylethanol	0	0	0	0	0	0	0	0	100	0	0	0	0	0	0	0	0	0	49	52
S-1-phenylethanol	0	0	0	0	0	0	0	0	0	100	0	0	0	0	0	0	0	0	51	48

Figure S11: a) and d) Confusion matrixes of the discrimination of the isomers of the odor molecules based on the data of the entire sensor array, i.e. all six sensors, see Fig.3 or table S1. b) and e) Confusion matrixes of the discrimination of the isomers of the odor molecules only based on the data from all three chiral sensors (left) and all three achiral sensors (right). Green are correct classifications, red are false classifications. All numbers are given in %. c) and f) The accuracy for the discrimination of the sensor data measured at different time intervals. Each value is determined from 40 consecutive data points, where the final points end at the values shown in the *x*-axis. The data for 10 ppm are on the left-hand side (a-c), 100 ppm on the right-hand side (d-f).

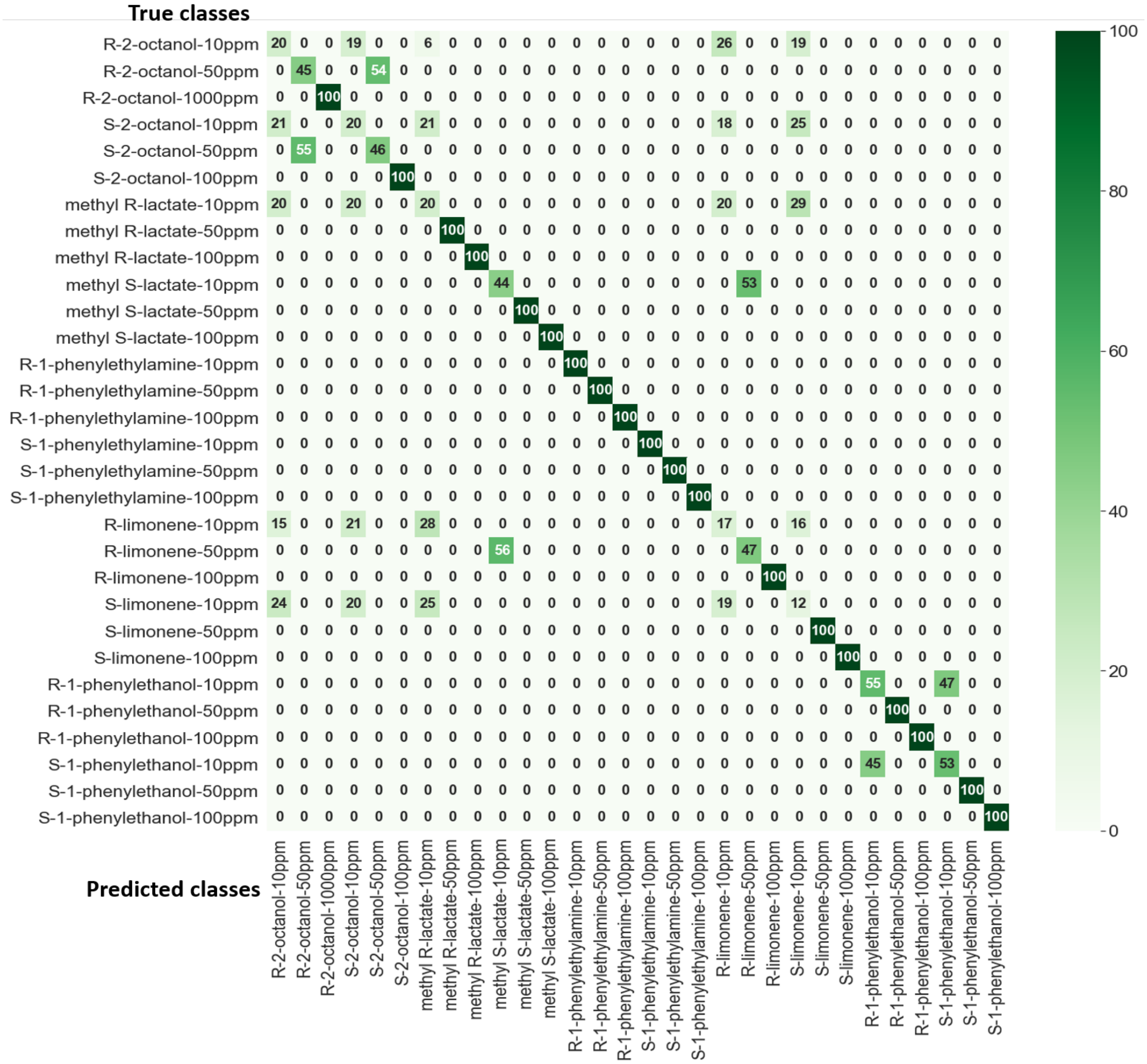

	R-2-octanol-10ppm	R-2-octanol-50ppm	R-2-octanol-1000ppm	S-2-octanol-10ppm	S-2-octanol-50ppm	S-2-octanol-100ppm	methyl R-lactate-10ppm	methyl R-lactate-50ppm	methyl R-lactate-100ppm	methyl S-lactate-10ppm	methyl S-lactate-50ppm	methyl S-lactate-100ppm	R-1-phenylethylamine-10ppm	R-1-phenylethylamine-50ppm	R-1-phenylethylamine-100ppm	S-1-phenylethylamine-10ppm	S-1-phenylethylamine-50ppm	S-1-phenylethylamine-100ppm	R-limonene-10ppm	R-limonene-50ppm	R-limonene-100ppm	S-limonene-10ppm	S-limonene-50ppm	S-limonene-100ppm	R-1-phenylethanol-10ppm	R-1-phenylethanol-50ppm	R-1-phenylethanol-100ppm	S-1-phenylethanol-10ppm	S-1-phenylethanol-50ppm	S-1-phenylethanol-100ppm
R-2-octanol-10ppm	20	0	0	19	0	0	6	0	0	0	0	0	0	0	0	0	0	0	26	0	0	19	0	0	0	0	0	0	0	0
R-2-octanol-50ppm	0	45	0	0	54	0	0	0	0	0	0	0	0	0	0	0	0	0	0	0	0	0	0	0	0	0	0	0	0	0
R-2-octanol-1000ppm	0	0	100	0	0	0	0	0	0	0	0	0	0	0	0	0	0	0	0	0	0	0	0	0	0	0	0	0	0	0
S-2-octanol-10ppm	21	0	0	20	0	0	21	0	0	0	0	0	0	0	0	0	0	0	18	0	0	25	0	0	0	0	0	0	0	0
S-2-octanol-50ppm	0	55	0	0	46	0	0	0	0	0	0	0	0	0	0	0	0	0	0	0	0	0	0	0	0	0	0	0	0	0
S-2-octanol-100ppm	0	0	0	0	0	100	0	0	0	0	0	0	0	0	0	0	0	0	0	0	0	0	0	0	0	0	0	0	0	0
methyl R-lactate-10ppm	20	0	0	20	0	0	20	0	0	0	0	0	0	0	0	0	0	0	20	0	0	29	0	0	0	0	0	0	0	0
methyl R-lactate-50ppm	0	0	0	0	0	0	0	100	0	0	0	0	0	0	0	0	0	0	0	0	0	0	0	0	0	0	0	0	0	0
methyl R-lactate-100ppm	0	0	0	0	0	0	0	0	100	0	0	0	0	0	0	0	0	0	0	0	0	0	0	0	0	0	0	0	0	0
methyl S-lactate-10ppm	0	0	0	0	0	0	0	0	0	44	0	0	0	0	0	0	0	0	0	53	0	0	0	0	0	0	0	0	0	0
methyl S-lactate-50ppm	0	0	0	0	0	0	0	0	0	0	100	0	0	0	0	0	0	0	0	0	0	0	0	0	0	0	0	0	0	0
methyl S-lactate-100ppm	0	0	0	0	0	0	0	0	0	0	0	100	0	0	0	0	0	0	0	0	0	0	0	0	0	0	0	0	0	0
R-1-phenylethylamine-10ppm	0	0	0	0	0	0	0	0	0	0	0	0	100	0	0	0	0	0	0	0	0	0	0	0	0	0	0	0	0	0
R-1-phenylethylamine-50ppm	0	0	0	0	0	0	0	0	0	0	0	0	0	100	0	0	0	0	0	0	0	0	0	0	0	0	0	0	0	0
R-1-phenylethylamine-100ppm	0	0	0	0	0	0	0	0	0	0	0	0	0	0	100	0	0	0	0	0	0	0	0	0	0	0	0	0	0	0
S-1-phenylethylamine-10ppm	0	0	0	0	0	0	0	0	0	0	0	0	0	0	0	100	0	0	0	0	0	0	0	0	0	0	0	0	0	0
S-1-phenylethylamine-50ppm	0	0	0	0	0	0	0	0	0	0	0	0	0	0	0	0	100	0	0	0	0	0	0	0	0	0	0	0	0	0
S-1-phenylethylamine-100ppm	0	0	0	0	0	0	0	0	0	0	0	0	0	0	0	0	0	100	0	0	0	0	0	0	0	0	0	0	0	0
R-limonene-10ppm	15	0	0	21	0	0	28	0	0	0	0	0	0	0	0	0	0	0	17	0	0	16	0	0	0	0	0	0	0	0
R-limonene-50ppm	0	0	0	0	0	0	0	0	0	56	0	0	0	0	0	0	0	0	0	47	0	0	0	0	0	0	0	0	0	0
R-limonene-100ppm	0	0	0	0	0	0	0	0	0	0	0	0	0	0	0	0	0	0	0	0	100	0	0	0	0	0	0	0	0	0
S-limonene-10ppm	24	0	0	20	0	0	25	0	0	0	0	0	0	0	0	0	0	0	19	0	0	12	0	0	0	0	0	0	0	0
S-limonene-50ppm	0	0	0	0	0	0	0	0	0	0	0	0	0	0	0	0	0	0	0	0	0	0	100	0	0	0	0	0	0	0
S-limonene-100ppm	0	0	0	0	0	0	0	0	0	0	0	0	0	0	0	0	0	0	0	0	0	0	0	100	0	0	0	0	0	0
R-1-phenylethanol-10ppm	0	0	0	0	0	0	0	0	0	0	0	0	0	0	0	0	0	0	0	0	0	0	0	0	55	0	0	47	0	0
R-1-phenylethanol-50ppm	0	0	0	0	0	0	0	0	0	0	0	0	0	0	0	0	0	0	0	0	0	0	0	0	0	100	0	0	0	0
R-1-phenylethanol-100ppm	0	0	0	0	0	0	0	0	0	0	0	0	0	0	0	0	0	0	0	0	0	0	0	0	0	0	100	0	0	0
S-1-phenylethanol-10ppm	0	0	0	0	0	0	0	0	0	0	0	0	0	0	0	0	0	0	0	0	0	0	0	0	45	0	0	53	0	0
S-1-phenylethanol-50ppm	0	0	0	0	0	0	0	0	0	0	0	0	0	0	0	0	0	0	0	0	0	0	0	0	0	0	0	0	100	0
S-1-phenylethanol-100ppm	0	0	0	0	0	0	0	0	0	0	0	0	0	0	0	0	0	0	0	0	0	0	0	0	0	0	0	0	0	100

Figure S12: Confusion matrixes for the classification of the enantiomers of the 5 chiral molecular pairs at three different concentrations, that means 30 classes. The average accuracy is 75.9 %.

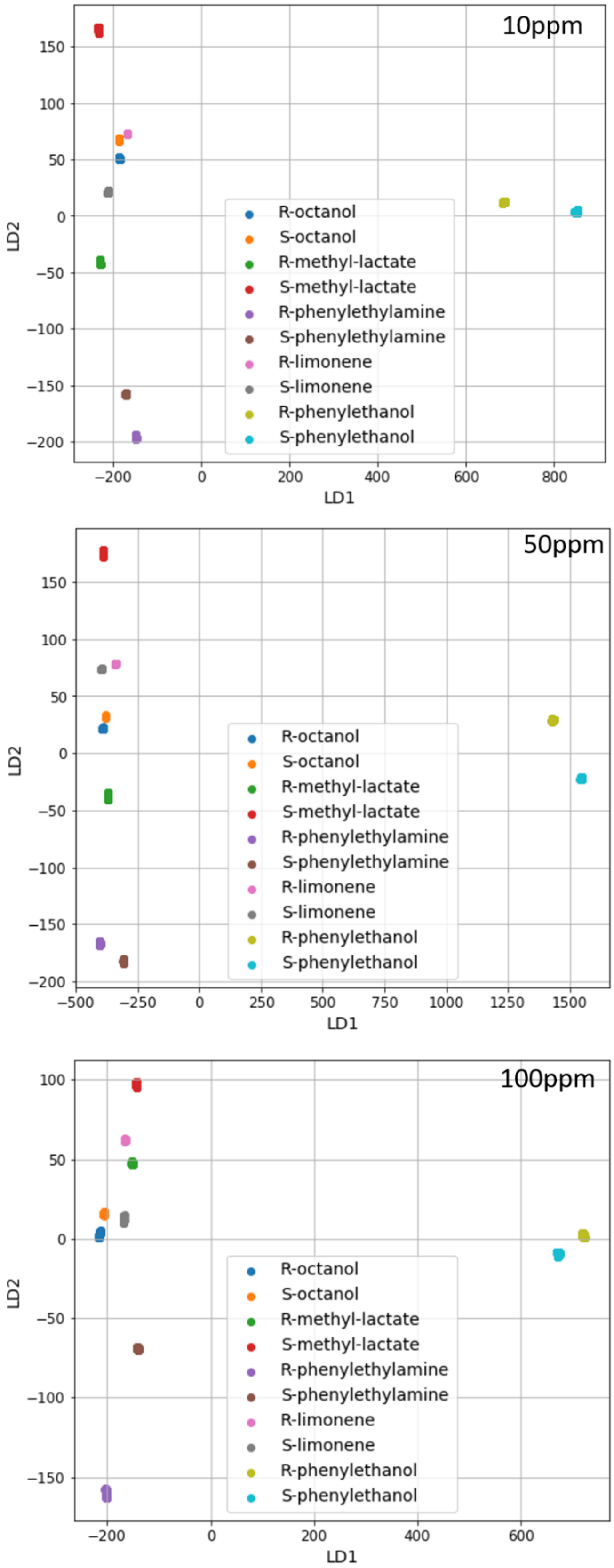

Figure S13: Linear discriminant analysis (LDA) of the sensor data recorded at 10 ppm (top), 50 ppm (center), 100 ppm (bottom) with the entire sensor array (that is all six sensors). The axes are the linear discriminants LD1 and LD2. The molecules are labelled in the legend.
The plots show that the data from the sensor array also allows a clear discrimination based on LDA.

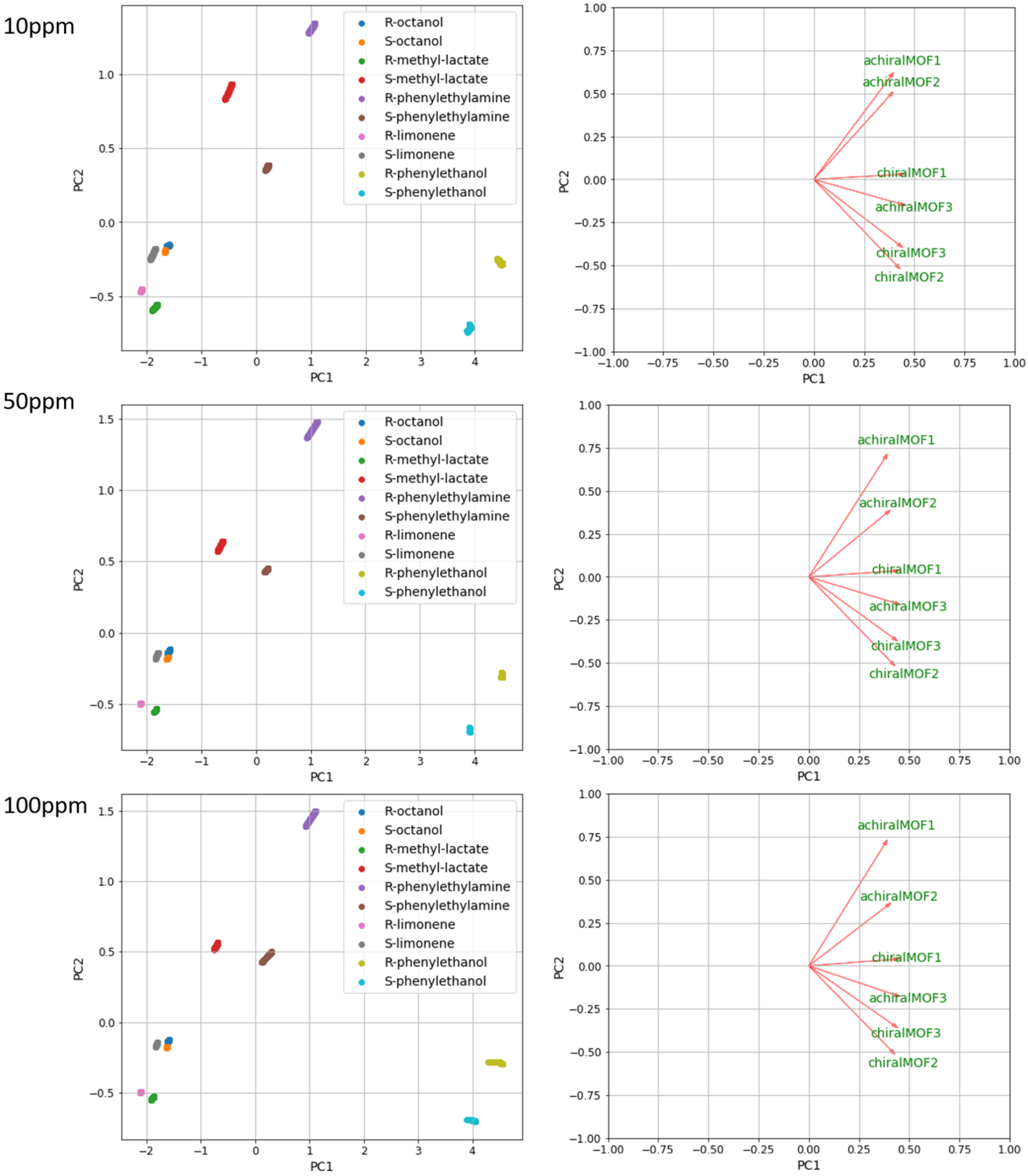

Figure S14: Principal component analysis (PCA) of the sensor data recorded at 10 ppm (top), 50 ppm (center), 100 ppm (bottom) with the entire sensor array (that is all six sensors). The score plots are shown on the left-hand side, the loadings plots are shown on the right-hand side. The axes are the principal components PC1 and PC2. The molecules and the MOF-sensors are labelled in the legend. The plots show that the data from the sensor array also allows a clear discrimination based on PCA.

References

[1] O. Shekhah, H. Wang, S. Kowarik, F. Schreiber, M. Paulus, M. Tolan, C. Sternemann, F. Evers, D. Zacher, R. A. Fischer, C. Wöll, *J. Am. Chem. Soc.* **2007**, *129*, 15118-15119.

[2] a) H. K. Arslan, O. Shekhah, J. Wohlgemuth, M. Franzreb, R. A. Fischer, C. Wöll, *Adv. Funct. Mater.* **2011**, *21*, 4228-4231; b) S. Hurrle, S. Friebe, J. Wohlgemuth, C. Wöll, J. Caro, L. Heinke, *Chem. Eur. J.* **2017**, *23*, 2294-2298.

[3] S. S. Y. Chui, S. M. F. Lo, J. P. H. Charmant, A. G. Orpen, I. D. Williams, *Science* **1999**, *283*, 1148-1150.

[4] J. X. Liu, B. Lukose, O. Shekhah, H. K. Arslan, P. Weidler, H. Gliemann, S. Bräse, S. Grosjean, A. Godt, X. L. Feng, K. Mullen, I. B. Magdau, T. Heine, C. Wöll, *Scientific Reports* **2012**, *2*, 921.

[5] D. N. Dybtsev, M. P. Yutkin, E. V. Peresypkina, A. V. Virovets, C. Serre, G. Ferey, V. P. Fedin, *Inorg. Chem.* **2007**, *46*, 6843-6845.

[6] C. A. E. S. Muckley, C. B. Jacobs, T. Hianik and I. N. Ivanov, *SPIE Organic Photonics+Electronics, Int. Soc. Opt. Photonics* **2016**, 99440Y

[7] G. Sauerbrey, G. Jung, *Z Angew Physik* **1968**, *24*, 100-+.

[8] a) G. Bolla, A. S. Myerson, *Crystengcomm* **2018**, *20*, 2084-2088; b) V. Stavila, J. Volponi, A. M. Katzenmeyer, M. C. Dixon, M. D. Allendorf, *Chem. Sci.* **2012**, *3*, 1531-1540.

[9] L. Heinke, *Journal of Physics D: Applied Physics* **2017**, *50*, 193004.

[10] a) S. Guney, A. Atasoy, *Sens. Actuator B-Chem.* **2012**, *166*, 721-725; b) K. T. Tang, Y. S. Lin, J. M. Shyu, *Sensors* **2010**, *10*, 10467-10483.

[11] S. Okur, Z. Zhang, M. Sarheed, P. Nick, U. Lemmer, L. Heinke, *Sensors & Actuators: B. Chemical* **2020**, *306*, 127502.

[12] a) B. Szulczynski, K. Arminski, J. Namiesnik, J. Gebicki, *Sensors* **2018**, *18*, 17; b) L. Zhang, F. Tian, D. Zhang, *Electronic Nose: Algorithmic Challenges*, **2018**; c) X. Zhao, Z. Wen, X. Pan, W. Ye, A. Bermak, *Ieee Access* **2019**, *7*, 12630-12637.

[13] a) M. Tu, S. Wannapaiboon, R. A. Fischer, *Dalt. Trans.* **2013**, *42*, 16029-16035; b) M. Tu, R. A. Fischer, *J. Mat. Chem. A* **2014**, *2*, 2018-2022; c) Q. Li, J. Gies, X.-J. Yu, Y. Gu, A. Terfort, M. Kind, *Chem. Eur. J.* **2020**, *26*, 5185-5189.

[14] Z.-G. Gu, A. Pfriem, S. Hamsch, H. Breitwieser, J. Wohlgemuth, L. Heinke, H. Gliemann, C. Wöll, *Micropor. Mesopor. Mat.* **2015**, *211*, 82-87.

[15] D. Bradshaw, T. J. Prior, E. J. Cussen, J. B. Claridge, M. J. Rosseinsky, *J. Am. Chem. Soc.* **2004**, *126*, 6106-6114.

[16] a) X. Bao, L. J. Broadbelt, R. Q. Snurr, *Micropor. Mesopor. Mat.* **2012**, *157*, 118-123; b) X. Bao, L. J. Broadbelt, R. Q. Snurr, *Phys. Chem. Chem. Phys.* **2010**, *12*, 6466-6473; c) R. Bueno-Perez, A. Martin-Calvo, P. Gomez-Alvarez, J. J. Gutierrez-Sevillano, P. J. Merkling, T. J. H. Vlugt, T. S. van Erp, D. Dubbeldam, S. Calero, *Chem. Comm.* **2014**, *50*, 10849-10852.

[17] a) S. E. Friberg , Q. Yin , P. A. Aikens *International Journal of Cosmetic Science* **1998**, *20*, 355-367; b) R. Krishna, *Phys. Chem. Chem. Phys.* **2016**, *18*, 15482-15495.

[18] a) M. Cakici, Z.-G. Gu, M. Nieger, J. Burck, L. Heinke, S. Bräse, *Chem. Comm.* **2015**, *51*, 4796-4798; b) Z. Gu, S. Grosjean, S. Bräse, C. Wöll, L. Heinke, *Chem. Comm.* **2015**, *51*, 8998-9001; c) O. Zybaylo, O. Shekhah, H. Wang, M. Tafipolsky, R. Schmid, D. Johannsmann, C. Wöll, *Phys. Chem. Chem. Phys.* **2010**, *12*, 8092-8097; d) A. B. Kanj, J. Buerck, S. Grosjean, S. Braese, L. Heinke, *Chem. Comm.* **2019**, *55*, 8776-8779.

[19] a) J. Kärger, D. M. Ruthven, D. N. Theodorou, *Diffusion in Nanoporous Materials*, Wiley-VCH, **2012**; b) K. Müller, N. Vankova, L. Schottner, T. Heine, L. Heinke, *Chem. Sci.* **2019**, *10*, 153-160; c) J. C. Saint Remi, A. Lauerer, C. Chmelik, I. Vandendael, H. Terryn, G. V. Baron, J. F. M. Denayer, J. Kärger, *Nat. Mater.* **2016**, *15*, 401-406; d) L. Heinke, Z. Gu, C. Wöll, *Nat. Comm.* **2014**, *5*, 4562; e) J. Kärger, *Micropor. Mesopor. Mat.* **2014**, *189*, 126-135; f) J. Kärger, T. Binder, C. Chmelik, F. Hibbe, H. Krautscheid, R. Krishna, J. Weitkamp, *Nat Mater* **2014**, *13*, 333-343; g) L. Heinke, J. Kärger, *Phys. Rev. Lett.* **2011**, *106*.

Author Contributions

SO and LH planned the project and the experiments. CL and ZZ prepared the SURMOF samples. SO performed the sensor experiments. PQ and AC analyzed the data. CL, ZZ, PQ and AC performed the XRD and SEM measurements. LH wrote the manuscript. All authors contributed and agreed to the final version of the manuscript.